This paper is the accepted version of the paper published on IEEE Transactions On Geoscience And Remote Sensing, Vol. 53, No. 12, Dec. 2015
Digital Object Identifier 10.1109/TGRS.2015.2444422

The Effect of Boreal Forest Canopy in Satellite Snow Mapping—A Multisensor Analysis

Juval Cohen, Juha Lemmetyinen, Jouni Pulliainen, *Senior Member, IEEE*, Kirsikka Heinilä, Francesco Montomoli, Jaakko Seppänen, and Martti T. Hallikainen, *Fellow, IEEE*

***Abstract*—Satellite-based snow-cover monitoring is performed using optical, synthetic aperture radar (SAR), and passive-microwave sensors. Effects of forest canopy on the observed signal need to be considered with all of these sensor types. Various models describing the interaction of electromagnetic radiation with forest canopy have been developed, but many of these are overly complex with high computational and ancillary data requirements. However, for retrieval purposes, simple models are preferred. This work aims at increasing the understanding of the effect of forest canopy on remote sensing observations of snow-covered terrain for both microwave and optical regimes and at quantifying the capability of simple zeroth-order models in simulating these effects. To achieve these goals, a spatial analysis of optical, SAR, and passive-microwave remote sensing data in the northern boreal forest region was performed. Model parameters for vegetation transmissivity as well as the properties of the underlying surface were optimized by utilizing lidar-ranging- and Landsat-based simplified proxy parameters describing forest canopy closure and stem volume. The results demonstrated that despite using these relatively simple proxies, a zeroth-order model can accurately estimate the extinction of electromagnetic signals in a forest, particularly for passive microwave and optical data. The SAR model successfully estimated the median of the observations, but larger scatter of the observations was reflected by a higher root mean square error and lower correlation between models and observations. Due to both good estimation accuracy and simplicity, the presented models can be considered to be applicable in existing snow retrieval algorithms.**

***Index Terms*—Boreal forest, optical, passive microwave, remote sensing of snow, synthetic aperture radar (SAR), snow, transmissivity.**

I. Introduction

INFORMATION regarding snow cover is essential for hydrological modeling, estimation of fresh water budget, weather prediction, and climate change studies [1]–[4]. Spaceborne remote sensing by optical or microwave instruments provides a cost-efficient tool for snow-cover monitoring globally, regionally, and on a local scale. One of the problems that reduce the feasibility of remote sensing is the effect of forest canopy on the observed signal. The topic of this study was to model and quantify these effects using a simple zeroth-order approach, applicable for retrieval of geophysical parameters from spaceborne observations.

The total mass of snow on the ground is usually expressed as snow water equivalent (SWE), which describes the amount of liquid water in a snowpack if melted. In case of patchy snow cover, fractional snow cover (FSC) defines the percentage of snow-covered area (SCA) from the total area. Sensor types used in snow-cover mapping include 1) optical, 2) active-microwave, and 3) passive-microwave sensors. The choice of the appropriate sensor is based on the requirements and the environmental conditions, such as the requested snow variable (SWE or FSC), geographical location and meteorological conditions of the observed area, the desired temporal and spatial resolution, and the cost of the satellite data. Available methods for snow-cover mapping with different sensor types have been reviewed in [5]–[7].

Optical satellite sensors are typically used for FSC mapping [8]–[17], but these can only be applied to determine whether snow is present or not; optical imagery cannot directly differentiate between deep and shallow snow. FSC estimation accuracy is typically high [16], [18] due to the high reflectance of snow in the optical and near-infrared (NIR) wavelengths compared with the reflectance of snow-free ground. The good availability of optical images from various sensors enables a high temporal resolution of observations, although the usability of optical data is highly dependent on cloud and lighting conditions. Therefore, in practice, long periods cannot be observed, particularly in frequently clouded areas with limited sunlight, such as the Arctic and subarctic.

An alternative to the optical sensors in FSC mapping is the use of active-microwave remote sensing, which is independent of meteorological conditions and time of day. Synthetic aperture radar (SAR) is the most common active-microwave sensor type used in FSC mapping [19]–[21]. Due to the presence of water in the snowpack, which increases the dielectric contrast at the air/snow interface, the backscattering signal from wet snow is considerably lower than the signal from snow-free ground or dry snow. The backscattering coefficient is therefore linearly dependent on the SCA for wet snow. The major advantage of SAR sensors, compared with optical, is the inherent sensitivity to cloud conditions. However, the availability of data is limited due to the relatively narrow swath and rarity of suitable sensors.

J. Cohen, J. Lemmetyinen, and J. Pulliainen are with the Finnish Meteorological Institute, 00101 Helsinki, Finland (e-mail: juval.cohen@fmi.fi; juval.cohen@gmail.com; juha.lemmetyinen@fmi.fi; jouni.pulliainen@fmi.fi).

K. Heinilä is with the Finnish Environment Institute, 00251 Helsinki, Finland (e-mail: kirsikka.heinila@ymparisto.fi).

F. Montomoli is with IFAC-CNR, Institute for Applied Physics, 50019 Sesto Fiorentino, Italy (e-mail: f.montomoli@ifac.cnr.it).

J. Seppänen and M. T. Hallikainen are with the School of Electrical Engineering, Aalto University, 00076 Espoo, Finland (e-mail: jaakko.seppanen@aalto.fi; martti.hallikainen@aalto.fi).

Color versions of one or more of the figures in this paper are available online at http://ieeexplore.ieee.org.

Digital Object Identifier 10.1109/TGRS.2015.2444422

However, emerging satellite systems, such as Sentinel-1, substantially increase the availability of SAR data.

Passive-microwave satellite sensors are suitable for SWE retrieval in dry-snow conditions. Most of the SWE retrieval algorithms exploit the difference between measured Tb at $\sim$19 GHz, which is largely insensitive to scattering effects of snow, and at $\sim$37 GHz, which is sensitive to volume scattering caused by snow grains. The absolute difference between these channels is positively correlated with SWE and can be exploited to produce regional and global estimates [22]–[25]. The main advantages in using passive-microwave sensors are good temporal resolution due to high revisit times and a large swath width, insensitivity of the microwaves to meteorological conditions and the time of day, as well as a time series of daily observations extending several decades [25]. However, as a main drawback, the spatial resolution of spaceborne microwave sensors is relatively coarse ($\sim$10–20 km), decreasing retrieval capabilities for heterogeneous satellite scenes. Wet snow also absorbs microwaves efficiently, preventing the detection of SWE in other than completely dry-snow conditions. However, wet snow can also be exploited in passive-microwave radiometry to analyze the onset of snow melt and the occurrence of snow clearance [26].

A large portion of areas that experience seasonal snow cover are located in the boreal forest region. Forest cover affects the observed signatures of both optical and microwave instruments. The albedo of the forest canopy is considerably lower than the albedo of snow, and therefore, forest canopy decreases the total reflectance of the snow-covered ground [27]–[33]. In active-microwave remote sensing with the L- , C-, or X-band radar, the forest canopy above wet snow typically increases the backscattering coefficient, due to volume scattering within the canopy itself [20], [34]–[37]. In passive-microwave remote sensing, the forest canopy attenuates emission from the snow and ground, while adding its own contribution to the emitted radiation. The measured brightness temperature of forested areas is typically higher than that of snow-covered open terrain [38]–[44]. Therefore, to correctly estimate the snow cover, it is essential to determine the quantitative influence of forest cover on the remote sensing signal for each sensor type.

Various models have been reported in the literature, describing both the optical and microwave properties of a forest canopy in remote-sensing-based snow retrieval. The developed models describing microwave interactions with vegetation can be roughly divided into two groups: empirical and analytical. Empirical models (e.g., [45] and [46]) aim to find a relationship between the measured backscatter coefficient and the properties of vegetation, e.g., canopy height, canopy volumetric moisture, and biomass, by optimizing empirical coefficients using statistical fitting. Empirical models are relatively simple, and the obtained accuracy for a given test case can be high, but generalization of the models for different vegetation types and environments is difficult. Analytical models, on the other hand, aim to estimate the backscatter based on modeling of the forest canopy and the interaction between vegetation and electromagnetic waves. Incoherent analytical models [47]–[57] consider only the intensity of the signal and need a rough description of the forest. Coherent analytical models [58], [59] use the intensity and the phase information of the signal and require more detailed inputs on the properties of the scattering media (i.e., forest canopy). Similarly, models describing the extinction of microwave radiation have been developed for purposes of passive-microwave remote sensing [38], [42], [44].

As discussed in [33], optical wavelength models can be divided into three basic approaches: 1) geometrical optics (GO), which assumes that tree canopies are opaque [9]–[11], [17], [30], [60], [61]; 2) radiative transfer (RT) models, where the canopy layer is considered as being partially transparent [14], [15], [62]; and 3) hybrid models, which combine RT for considering trees and GO to account for openings between the trees [27]–[29], [31], [63].

Practical retrieval schemes applying Earth Observation (EO) data to retrieve snow-cover parameters (e.g., [15], [25], and [64]) place stringent requirements on the compensation for forest cover effects. The applied methodology or model cannot be overly complex due to the inherent high requirements of ancillary data needed by, e.g., most analytical models. Therefore, simple models with limited ancillary data and computing requirements are preferred for retrieval purposes. The aim of this work was to analyze and increase the understanding of the effect of forest canopy on remote sensing observations of snow-covered terrain for both the microwave and optical regimes and to quantify the capability of simple zeroth-order models in simulating these effects under snow-cover conditions. In particular, the research had the following objectives:

1) to consistently analyze the effect of forest canopy on active- and passive-microwave remote sensing and optical observations of snow-covered terrain;
2) to estimate the feasibility of a zeroth-order model in simulating the observed forest canopy effects for all three sensor types, using available forestry information [canopy closure (CC) and forest stem volume (SV)] to drive the model.

To achieve these goals, a spatial analysis of various airborne and spaceborne remote sensing data at a dedicated test site in the northern boreal forest region was performed. The forest contribution was first analyzed for an optical sensor, then for X- and Ku-band active-microwave sensors, and finally for passive-microwave sensors ranging from X- to Ka-bands. The models were applied in an iterative inversion scheme to retrieve an estimate of the signal beneath the forest canopy, which was compared with measurements made over nonvegetated terrain in the same area. In the following sections, a short description of the test area and the used data sets and model are given, followed by the results of the data analysis for each sensor type and conclusions.

II. Test Area and Data

Data collection was performed over a test site near Sodankylä, Northern Finland (see Fig. 1). The collected data set consists of four different EO data sets: 1) airborne optical; 2) airborne active-microwave; 3) spaceborne active-microwave; and 4) airborne passive-microwave data (see Fig. 1). In addition, airborne light detection and ranging (LiDAR) measurements were used to derive the forest properties, such as CC, tree height (TH), and SV.

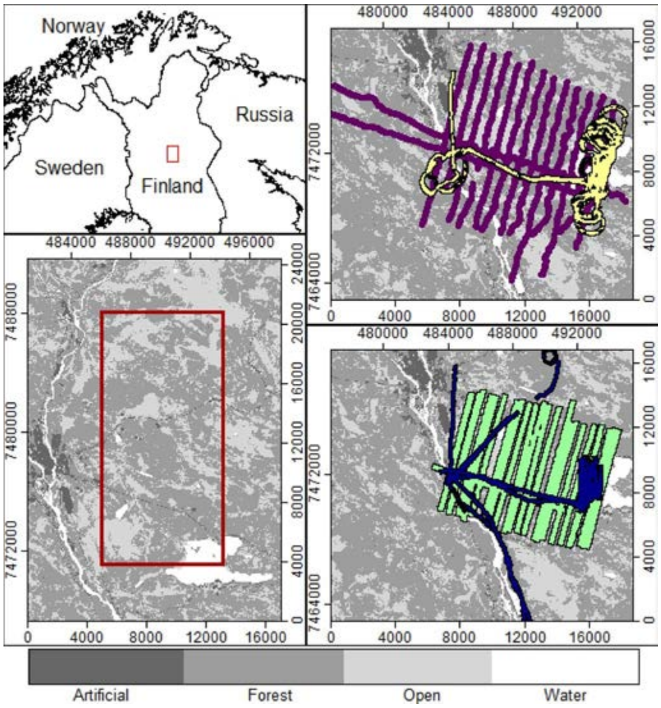

Fig. 1. All analyzed data. Upper left: Location of the Sodankylä test area on a large scale map. Lower left: Red frame shows the area that was analyzed from the TSX acquisitions. Upper Right: Light-yellow areas were scanned by the AISA spectrometer on 21.3.2010, and dark-purple areas were scanned by the Helsinki University of Technology Radiometer (HUTRAD) on 17.3.2011. Lower right: Dark-blue areas were scanned by AISA on 18.3.2010, and light-green areas were scanned by the SnowSAR instrument on 7.2.2012. UTM coordinates are shown on the upper-left side of the images, and the image length in meters is shown on the lower-right side of the images.

The most prominent land cover in the region consists of coniferous boreal forests (mainly Scots pine), wetlands, and lakes. The portion of Scots pine, spruce, birch, and other deciduous trees from the total tree SV in the test area is 73.0%, 13.3%, 13.3%, and 0.2%, respectively (Finnish Forest Research Institute, 2013). In the histograms of Fig. 2, the CC, TH, and SV distributions in the scanned areas of the AISA, SnowSAR, TSX, and HUTRAD sensors are shown. Winter (December–February) and summer (June–August) average air temperatures in the area are -12.6 °C and 12.6 °C, respectively. Snow cover typically persists for six to seven months during winter, and the average snow depth at the end of March is between 60 and 80 cm (statistics for the reference period of 1981–2010: [65]).

A. Optical Data

The optical wavelength data set was acquired with the AisaDUAL instrument (see Table I), which was installed in a helicopter. The instrument combines two sensors and provides very high spatial and spectral resolution data. The spectral range and resolution were 400–970 and 5 nm for the optical sensor and 970–2500 and 6 nm for the SWIR sensor, respectively. The flight altitude of the helicopter was 800 m, which produced a spatial resolution of 0.8 m on the ground. The acquired swath width was 240 m, with acquisitions extending over several kilometers (see Fig. 1). The campaign was carried out between the 18th and the 21st of March 2010, in ideal weather and snow

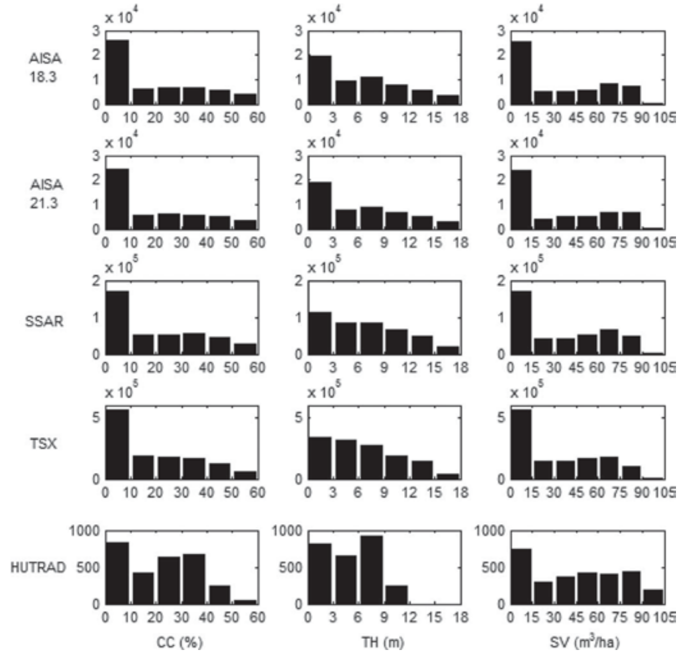

Fig. 2. CC, TH, and SV in the areas scanned by the different sensors. The y-axis shows the number of observations for each CC, TH, or SV interval.

TABLE I
AISA INSTRUMENT DETAILS

Date and time of acquisition	18.3.2010, 10:05 UTC	21.3.2010, 10:05 UTC
Snow Depth (cm)	77	83
Solar zenith angle (°)	68.3	67.1
Solar azimuth angle (°)	175.5	175.7
Look angle, off nadir (°)	-8.5 - +8.5	-8.5 - +8.5
Snow surface temperature (°C)	-6	-7
Air temperature (°C)	-4	-5

conditions, i.e., subzero temperatures and clear-sky conditions close to the peak snow season (100% dry-snow-cover conditions). On the 18th of March, the tree canopies were snow free, and snow cover on the ground was several days old, whereas on the 21st of March, the ground and the canopies were covered by newly fallen snow. All measurements were carried out in direct illumination (i.e., clear sky: 0/8 to 2/8 cloud cover). The instrument foreoptics unit was set to look at nadir (0°) direction, and the field of view was 17°. A more detailed description of the AISA instrument and acquisitions has been given in [32].

AISA data were radiometrically and geometrically corrected using ENVI software. First, the images were filtered with a mean filter using a 12×12 window size, corresponding to a pixel size of 10 m. Then, using the band-specific full-width-at-half-maximum criterion, AISA spectral bands were aggregated to correspond to MODIS bands 1 (red, 620–670 nm), 2 (NIR, 841–876 nm), 3 (blue, 459–479 nm), and 4 (green, 545–565 nm).

B. SAR Data

The most comprehensive data sets in this study were spaceborne and airborne SAR data. These data were obtained within Phase A studies of the proposed Cold Regions Hydrology

TABLE II
TSX AND SNOWSAR INSTRUMENT DETAILS

Parameter	TerraSAR-X	SnowSAR
Incidence angle (°)	33.1 – 34.5	35 - 45
Frequency (GHz)	9.65 (X-band)	9.6 (X-band), 17.25 (Ku-band)
Resolution	up to 3m spatial resolution	Over 200 ENL over a ground surface area of 10 x 10 m
Polarization	VV + VH	VV + VH
Swath width	-	400 m
Flight altitude	-	1600 m

TABLE III
HUTRAD INSTRUMENT DETAILS

Frequency [GHz]	10.65	18.7	36.5
Bandwidth [MHz]	120	130	400
Sensitivity [K]	0.6		0.3
Accuracy [K]	<3		<1
θ_{3dB} [°]	3		4
Footprint size [m]	37 x 76		49 x 101
Incidence angle [°]	45-55		
Scan method	Along track		
Flight altitude [m]	600		

High-Resolution Observatory (CoReH2O) mission, one of the candidates for the 7th Earth Explorer Core mission by the European Space Agency (ESA) [64]. The collected SAR data include a whole-winter time series of TerraSAR-X dual-polarization (VV and VH) acquisitions from the winter of 2010–2013 and airborne X- and Ku-band dual-polarization (VV and VH) data from the winter of 2011–2012, acquired with the ESA SnowSAR instrument (see Table II). The airborne SnowSAR instrument was calibrated using a combination of internal calibration standards, trihedral reflectors placed on the test area, and a cross-comparison to TerraSAR-X observations [66]. In this paper, a single SnowSAR acquisition from 7.2.2012 was analyzed. The TerraSAR-X time series included 17 images from the winter of 2010–2011, 23 images from the winter of 2011–2012, and 13 images from the winter of 2012–2013. All SAR data were resampled from their original spatial resolution (2 m in SnowSAR and 3–5 m in TSX) to a 10-m resolution by calculating the mean value of the pixels.

C. Passive-Microwave Data

The passive-microwave data used in this study were acquired by the Department of Radio Science and Engineering of Aalto University, Finland, with the HUTRAD, between the 16th and the 18th of March 2011. HUTRAD (see Table III) measures in six frequencies (6.9, 10.65, 18.7, 23.8, 36.5, and 89.0 GHz) and in two polarizations (V and H). In this paper, frequencies 10.65, 18.7, and 36.5 GHz were examined, as these are the most relevant channels regarding the retrieval of snow-cover parameters. The airborne radiometer system was calibrated five times during the campaign, ideally before and after each measurement flight, using a two-point external calibration at the antenna reference frame (microwave absorbers at ambient temperature and cooled by liquid nitrogen). However, on the last day of measurements, a calibration was performed only after the flight. Based on the calibrations during the first two days of operations, the estimated instrument stability was ± 3 K for 10.65 and 18.7 GHz and ± 1 K for 36.5 GHz. The footprint size of one sample area on the ground (spatial resolution) at the flight altitude of 600 m, a nominal incidence angle of 50° and considering flat ground was 37 $\times$ 76 m for the 10.65- and 18.7-GHz bands, and 49 $\times$ 101 m for the 36.5-GHz band.

D. Forest Cover Data

Airborne laser scanning (ALS) data from the National Land Survey (NLS) of Finland was used to create CC and TH maps in a 10-m spatial resolution. The point density of these data is at least 0.5 points/m^2, which is equivalent to a distance of approximately 1.4 m between points. The scanning in the Sodankylä region was performed in May 2010, when deciduous trees were still leafless. The mean vertical and horizontal errors of the LiDAR points are up to 15 and 60 cm, respectively. The flight altitude was 2000 m, which creates a footprint area of 50 cm on the ground.

The first step in processing the LiDAR data was to create vegetation height (VH) grids with a pixel size of 1 m for CC retrieval and 2 m for TH retrieval. The VH grids were generated first by subtracting the ground-level height (Digital Terrain Model) from the top of VH (Digital Surface Model) and then by converting the resulted point cloud to grids of 1- and 2-m pixel size. Points with a scanning angle exceeding 20° were excluded. The second step was to generate the CC map from the 1-m VH grid and the TH map from the 2-m VH grid. The CC was generated by 1) classifying pixels to either tree or no-tree, 2) calculating the ratio between tree pixels and all pixels inside a grid cell of 10 $\times$ 10 m, and 3) applying a correction with respect to the scanning angle. The TH map was generated by 1) removing low vegetation and water, 2) applying a circle-shaped dilation (maximum) filter with a radius of 2 pixels (equivalent to 4 m on the ground), and 3) calculating the mean height inside a grid cell of 10 $\times$ 10 m. The retrieved maps were evaluated against corresponding Multi-Source National Forest Inventory (MS-NFI) data [67] at a spatial resolution of 20 m. The evaluation showed good correlation between ALS-based CC and TH and MS-NFI data (see Fig. 3).

SV was indirectly retrieved from the ALS data, by multiplying CC with TH (CCxTH), and comparing it with SV from MS-NFI data ($SV_{MS\text{-}NFI}$) (see Fig. 4). Linear and nonlinear exponential fitting of CCxTH to $SV_{MS\text{-}NFI}$ was tested, and the nonlinear fit was found to be better, which was expressed by a fit curve, i.e.,

$$SV_{MS\text{-}NFI} = 91(-e^{-0.0032\,CC\,TH}). \quad (1)$$

A possible source of bias in this SV estimation can be the presence of different tree species with a different tree structure. If, for instance, the diameter at breast height (DBH) of one tree species is typically larger than the DBH in other tree species, the same CC and TH would not give the same SV.

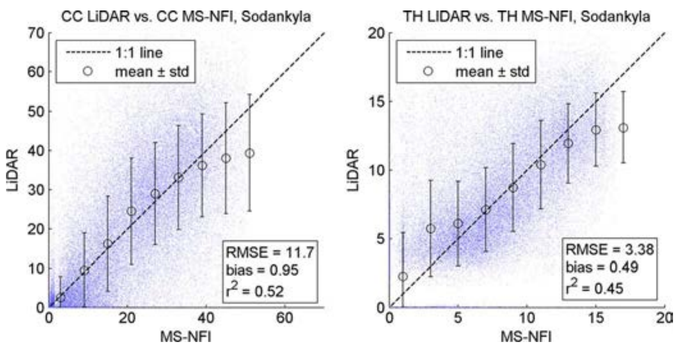

Fig. 3. LiDAR CC and TH maps evaluated against corresponding MS-NFI data sets. The root mean square error (RMSE) and bias show the deviation of the LiDAR data points from the 1:1 line, and the coefficient of determination shows the correlation between LiDAR and MS-NFI values.

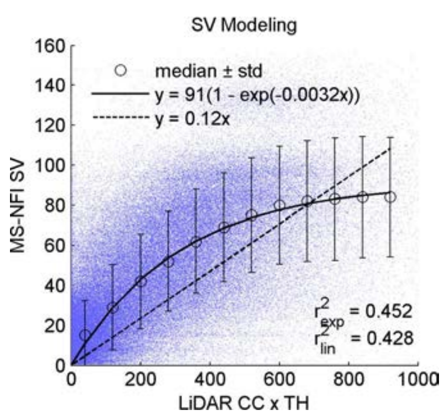

Fig. 4. Modeling of SV from LiDAR CC and TH. The exponential fit had a better correlation, lower RMSE, and smaller bias ($r^2 = 0.452$, RMSE = 24.1, bias = 3.95) compared with the linear fit ($r^2 = 0.428$, RMSE = 29.0, bias = 16.2).

TABLE IV
DBH AS A FUNCTION OF TH FOR SCOTS PINE, NORWAY SPRUCE, AND BIRCH [68]

Tree height (m)	DBH (cm)		
	Scots pine	Norway spruce	Birch
1.3-3	2.24	2.07	1.31
3-5	4.30	4.33	3.00
5-7	6.50	6.50	5.00
7-9	9.56	9.33	7.30
9-11	13.00	11.67	10.00
11-13	18.00	16.00	-

Measurements in the Northern part of Sweden [68] showed that pine and spruce had a similar relationship between TH and DBH, whereas the DBH of birches was, on average, 58%–86% from the DBH of pines and spruces (see Table IV). In our study region, 86.3% of the trees are pine or spruce, and only 13.3% are birch, and therefore, the bias due to different DBH values is expected to be small.

LiDAR-based forest maps were used when analyzing the data sets from AISA, SnowSAR, and TSX sensors, where the original spatial resolution was less than 10 m (before upscaling them to 10-m pixel size). In the HUTRAD data analysis, MS-NFI forest data were used because their spatial extent was larger than the spatial extent of the LiDAR forest maps, and they covered all HUTRAD scanned areas. Moreover, for HUTRAD, there was no need for forest maps in higher spatial resolution than 20 m. The pixel size in the optical and SAR analyses was thus 10 m, whereas in the passive-microwave analysis, it was approximately 37 × 76 m for the 10.65- and 18.7-GHz bands and 49 × 101 m for the 36.5-GHz band. The MS-NFI forest data used in the passive-microwave analysis were therefore averaged to the HUTRAD resolution, which is why it has relatively less large values, e.g., CC higher than 15% and TH higher than 12 m, as shown in Fig. 2. Zero values (treeless areas) were included in the histograms, and therefore, the lowest CC, TH, and SV interval was typically the highest.

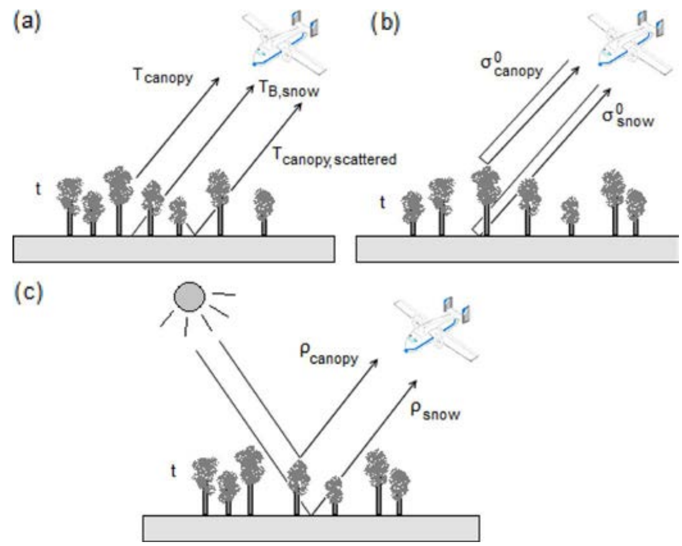

Fig. 5. Different (a) brightness temperature, (b) backscatter, and (c) reflectance contributions to the total radiation, which are considered in the models of this study, in (7), (8), and (9). (a) Passive microwave. (b) Active microwave. (c) Optical.

III. METHODOLOGY

Simplified zeroth-order models of the RT equations were applied to simulate the influence of the vegetation on the observed optical reflectance, microwave backscatter, and microwave emissivity. The components forming a zeroth-order forest model in each case are shown in Fig. 5.

A similar approach has been previously applied in the case of active and passive microwaves in, e.g., [35], [36], and [69] and in the case of optical data in [14], [15], and [33]. In this paper, the one-way transmissivity of the forest canopy is assumed to be exponentially related to the total extinction, so that

$$
\begin{aligned}
t_{\text{one-way}} &= e^{-K_e \mathrm{FP}/\cos\theta} \\
&= e^{-\kappa'_e \mathrm{FP}} \qquad (2)
\end{aligned}
$$

where K_e is the canopy extinction coefficient, κ'_e is the effective canopy extinction coefficient (canopy extinction coefficient divided by the cosine of the observation angle θ), and FP is a parameter describing the physical properties of the vegetation canopy (CC or SV in this study). In the optical and SAR models, two-way transmissivity is used, as the radiation passes through the forest canopy twice, i.e., once when propagating from the radiation source to the ground, and again, when propagating from the ground to the sensor after reflection at the ground interface. In the SAR model, the two-way transmissivity is considered as the one-way transmissivity defined in (2) to the second power, as the incoming and outgoing angles are the same (forest canopy conditions are considered equal for both propagation paths), i.e.,

$$t_{\text{two-way,SAR}} = t^2_{\text{one-way}} = e^{-2\kappa'_{e,\text{SAR}}\text{FP}}. \tag{3}$$

However, in the optical model, the incoming angle θ_{sun} and outgoing angle θ_{sensor} are different, and therefore, the two-way transmissivity is defined as

$$t_{\text{two-way,OPT}} = e^{-\frac{\kappa_e \text{FP}}{\cos\theta_{\text{sun}}} - \frac{\kappa_e \text{FP}}{\cos\theta_{\text{sensor}}}} = e^{-2\kappa'_{e,\text{OPT}}\text{FP}} \tag{4}$$

where

$$\kappa'_{e,\text{OPT}} = \frac{\kappa_e}{2}\left(\frac{1}{\cos\theta_{\text{sun}}} + \frac{1}{\cos\theta_{\text{sensor}}}\right). \tag{5}$$

The RT model for mixed forested and open-area observations is expressed as

$$a_{\text{total}} = \text{FF}a_{\text{forest}} + (1 - \text{FF})a_{\text{ground}} \tag{6}$$

where the forest fraction (FF) represents the fraction of forests in the sample area and can be between 0 and 1, a_{total} represents the total measured radiation at the sensor, and a_{forest} represents the radiation from forested areas and a_{ground} radiation from open areas. However, in this study, the model considers a sample area as being entirely nonforested or entirely forested with changing CC or SV; hence, the forest fraction for each sample area is considered to be either 0 (nonforested) or 1 (entirely forested). Regarding the optical and the active-microwave models, this assumption is acceptable because the pixel size was only 10 × 10 m after upscaling from the original resolution of 0.8 m in AISA, 2 m in SnowSAR, and 3–5 m in TSX. However, in the passive-microwave model, where the footstep size was 37 × 76 m for 10 and 18 GHz and 49 × 101 m for 36 GHz, the FF would often be somewhere between 0 and 1. Therefore, in the passive-microwave model, only samples with FF lower than 0.1 (nonforested) and higher than 0.7 (forested) were included in the analysis.

Next, the zeroth-order models for optical [see (7)] as well as active [see (8)] and passive [see (9)] microwave observations are described. The first term in (7)–(9) determines the contribution of snow on the ground, and the second term determines the contribution of the forest canopy on the observed signal. The third term in (9) determines the downwelling emission of the tree canopy, which is scattered from the ground toward the sensor.

A. Optical Forest Model

When applied for optical data, the zeroth-order total reflectance ρ observed above the forest canopy can be expressed as

$$\rho\left(\kappa'_{e,\text{OPT}}, \rho_{\text{snow}}, \rho_{\text{canopy}}\right) = t_{\text{two-way,OPT}}\rho_{\text{snow}} + (1 - t_{\text{two-way,OPT}})\rho_{\text{canopy}} \tag{7}$$

where ρ_{snow} is the reflectance of the snow (on the ground), and ρ_{canopy} is the reflectance of the canopy. The model thus neglects multiple scattering components, e.g., scattering in the atmosphere or between ground surface and the canopy layer.

B. Active-Microwave Model

Applying an analogous model as presented in (7) for the case of microwave backscatter gives

$$\sigma^0\left(\kappa'_{e,\text{SAR}}, \sigma^0_{\text{snow}}, \sigma^0_{\text{canopy}}\right) = t_{\text{two-way,SAR}}\sigma^0_{\text{snow}} + (1 - t_{\text{two-way,SAR}})\sigma^0_{\text{canopy}} \tag{8}$$

where σ^0 is the total backscatter, σ^0_{snow} is the backscattering coefficient of the snow/ground, and σ^0_{canopy} is the backscattering coefficient of the forest canopy. Optical and SAR thus behave both as active systems, where the radiation beam passes through the canopy layer twice. Multiple reflections and scattering effects between interfaces are neglected.

C. Passive-Microwave Model

For the passive-microwave sensor, one-way transmissivity (t) is used instead of the two-way transmissivity (t^2), because the radiation passes through the forest canopy only once. A third component is also added to the model, i.e., the emission of the canopy toward the ground, which is scattered from the ground to the sensor. The model for the passive-microwave case can be expressed as

$$\begin{aligned} T_B\left(\kappa'_{e,\text{PM}}, T_{B,\text{snow}}, T_{\text{canopy}}\right) &= t_{\text{one-way}}T_{B,\text{snow}} + (1 - t_{\text{one-way}})T_{\text{canopy}} \\ &\quad + (1 - t_{\text{one-way}})rt_{\text{one-way}}T_{\text{canopy}} \end{aligned} \tag{9}$$

where r is the reflectivity of the ground/snow approximated by

$$r = 1 - \frac{T_{B,\text{snow}}}{270}. \tag{10}$$

The passive-microwave zeroth-order model neglects the effects of other multiple reflections between, e.g., the atmosphere, the forest canopy, and the ground surface. Moreover, volume scattering within the canopy and scattering within different layers of the ground system are omitted.

D. Inversion Method

A numerical inversion method was implemented to the forward models for vegetation described in (7)–(10) to retrieve the ground-level signal beneath the forest canopy, i.e., $\rho_{\text{snow,ret}}$, $\sigma^0_{\text{snow,ret}}$, and $T_{B,\text{snow,ret}}$ (presented in (7)–(10) as: ρ_{snow}, σ^0_{snow}, and $T_{B,\text{snow}}$), free of the influence of vegetation. The method, applied in the literature for both optical and SAR data (e.g., [15] and [21]), exploits a large number of observations to iteratively fit the model against a suitable parameter describing vegetation properties. The free parameters in the optimization

$$
\min \left\{
\begin{array}{l}
\sum_{i=1}^{N} \left[\rho_{\mathrm{model},i}\left(\rho_{\mathrm{snow,ret}}, \rho_{\mathrm{canopy}}, \kappa'_{e,\mathrm{OPT}}, \mathrm{FP}_i\right) - \rho_{\mathrm{obs,median},i} \right]^2 \\
\sum_{i=1}^{N} \left[\sigma^0_{\mathrm{model},i}\left(\sigma^0_{\mathrm{snow,ret}}, \sigma^0_{\mathrm{canopy}}, \kappa'_{e,\mathrm{SAR}}, \mathrm{FP}_i\right) - \sigma^0_{\mathrm{obs,median},i} \right]^2 \\
\sum_{i=1}^{N} \left[T_{B,\mathrm{model},i}\left(T_{B,\mathrm{snow,ret}}, T_{\mathrm{canopy}}, \kappa'_{e,\mathrm{PM}}, \mathrm{FP}_i\right) - T_{B,\mathrm{obs,mean},i} \right]^2
\end{array}
\right\} \tag{11}
$$

effectively yield the required parameter, i.e., the signal emanating from beneath the forest canopy. In this paper, models were fit to the observational data using the method of least squares, minimizing the cost functions given in (11), shown at the top of the page, where FP refers to the used forest parameter (CC or SV), and i refers to the CC or the SV class. Three free parameters were applied in each model, whereas the FP was obtained from ancillary data. Free parameters considering the optical model were the contribution of open (nonforested) areas $\rho_{\mathrm{snow,ret}}$ and canopy ρ_{canopy} to the upwelling radiation as well as the canopy effective extinction coefficient $\kappa'_{e,\mathrm{OPT}}$. Correspondingly, the three free parameters in the SAR model were $\sigma^0_{\mathrm{snow,ret}}$, $\sigma^0_{\mathrm{canopy}}$, and $\kappa'_{e,\mathrm{SAR}}$, and those in the passive-microwave model were $T_{B,\mathrm{snow,ret}}$, T_{canopy}, and $\kappa'_{e,\mathrm{PM}}$.

The remote sensing observations were stratified into 10–12 CC classes or SV classes, depending on which one of the forest parameters was used in the model. The first class included observations where CC or SV was zero, the second class included observations where $0 < \mathrm{CC} <= 7$ or $0 < \mathrm{SV} < 10$. For all the following classes, the increase was 7 for CC and 10 for SV. For each CC or SV class, the mean or median reflectance ($\rho_{\mathrm{obs,median},i}$), backscatter ($\sigma^0_{\mathrm{obs,median},i}$), and brightness temperature ($T_{B,\mathrm{obs,median},i}$) values were calculated. The models were then fitted to the mean/median values of the selected CC or SV class. In case of SAR and optical data, minimization of (11) was performed against the median of observed values to minimize the effect of occasional very high or low backscatter/reflectance. In the passive-microwave observations, the standard deviation of the brightness temperature was relatively low, and therefore, the minimization was performed against mean values.

For all sensor types, the inversion was performed for both FP = CC and FP = SV. In the optical and SAR analyses, the forest data were derived from the LiDAR data, and in the passive microwave, the forest data were derived from the MS-NFI data, as explained in Section II-D. For model validation, the true contribution of the snow ground system in open areas ($\rho_{\mathrm{snow,obs}}$, $\sigma^0_{\mathrm{snow,obs}}$, and $T_{B,\mathrm{snow,obs}}$) was also computed based on the observations, by calculating the median (optical and active-microwave data) or mean (passive-microwave data) value of all observations where CC or SV was lower than 0.1. This inversion method can also be applied in actual implementation of the models for snow retrieval, providing that snow cover and vegetation transmissivity properties are considered to be constant over the area of interest. An analogous inversion process is applied for SAR data, e.g., in [21] and [36].

Some land cover areas that had a distorting effect on the signal were omitted from the analysis. For this purpose, land cover information was extracted from the Finnish Corine Land Cover 2006. In the passive-microwave analysis, an observation was not included if more than 20% of the footprint area was over urban areas or water bodies. In the SAR data analysis, only urban areas were removed. In the case of optical data analysis, however, all data points were included in the analysis due to the inherent high resolution of the data.

IV. Results

The forest models described in (7)–(9) were fitted to the observations of the optical (AISA), active-microwave (SnowSAR and TSX), and passive-microwave (HUTRAD) observations, respectively, using the inversion process explained in Section III [see (11)]. The inversion provided an estimate of the signal (reflectance, backscattering, or brightness temperature) emanating from beneath the forest canopy. The statistical fit of the model against the spread of observations with varying vegetation cover was analyzed. Furthermore, the retrieved estimate of the ground-level signal was compared with measurements over nonvegetated terrain. For all sensor types, the model inversion was performed against the two forest parameters, i.e., CC and SV.

A. Optical

Results of the optical forest model are summarized in Table V in terms of RMSE, bias error, coefficient of determination (r^2) between estimates of the model against observations, and the difference between observed and retrieved snow reflectance. The errors and correlations were about as high when using FP = CC or FP = SV. Moreover, the differences between retrieved and observed snow reflectance were similar. The results of the optical model for the AISA acquisitions from the 18th to the 21st of March 2010 are presented in Fig. 6 for four spectral bands. The retrieved values of $\rho_{\mathrm{snow,ret}}$, ρ_{canopy}, and $\kappa'_{e,\mathrm{OPT}}$ for the model in (7) are shown. For the first day of observations, snow reflectance values $\rho_{\mathrm{snow,obs}}$ between 0.80 and 0.88 were retrieved, whereas observed reflectance values over nonvegetated terrain $\rho_{\mathrm{snow,obs}}$ showed reflectance values between 0.82 and 0.9. For all four bands, $\rho_{\mathrm{snow,ret}}$ was thus very close to $\rho_{\mathrm{snow,obs}}$. For the second day of observations, $\rho_{\mathrm{snow,ret}}$ was also very close to $\rho_{\mathrm{snow,obs}}$ for all four spectral bands. All retrieved and observed reflectance values were higher in the second day of observations due to the newly fallen snow, with the exception of $\rho_{\mathrm{snow,obs}}$ and $\rho_{\mathrm{snow,ret}}$ for the NIR band. The mean r^2 value between modeled and observed reflectance was 0.74 for the first day as well as for the second day of observations, indicating that the model was well able to capture the dynamics of the reflectance signal with changing forest canopy conditions. The lowest correlations were observed on both days for the NIR spectral band.

TABLE V

RESULTS OF OPTICAL MODEL ESTIMATES AGAINST AIRBORNE AISA SPECTROMETER OBSERVATIONS (RMSE, BIAS, COEFFICIENT OF DETERMINATION, AND THE DIFFERENCE BETWEEN THE RETRIEVED AND THE OBSERVED SNOW REFLECTANCE IN OPEN AREAS) AT FOUR SPECTRAL BANDS (BLUE: 459–479 μm, GREEN: 545–565 μm, RED: 620–670 μm, NIR: 841–876 μm) WHEN USING FP = CC AND FP = SV

Date	Band	CC				SV			
		RMSE	bias	r^2	$\rho_{snow,obs} - \rho_{snow,ret}$	RMSE	bias	r^2	$\rho_{snow,obs} - \rho_{snow,ret}$
18.3	Blue	0.123	0.0009	0.79	0.02	0.121	-0.0043	0.79	0.02
	Green	0.126	0.0016	0.78	0.02	0.123	0.0009	0.78	0.03
	Red	0.125	0.0022	0.76	0.02	0.123	-0.0021	0.77	0.02
	NIR	0.137	0.0011	0.62	0.02	0.134	0.0018	0.64	0.02
21.3	Blue	0.127	-0.0042	0.72	0.00	0.125	-0.0053	0.73	0.00
	Green	0.136	-0.0101	0.73	0.00	0.133	-0.0080	0.74	0.01
	Red	0.128	-0.0097	0.80	0.01	0.125	-0.0092	0.81	0.02
	NIR	0.119	-0.0142	0.71	0.00	0.114	-0.0071	0.73	0.02

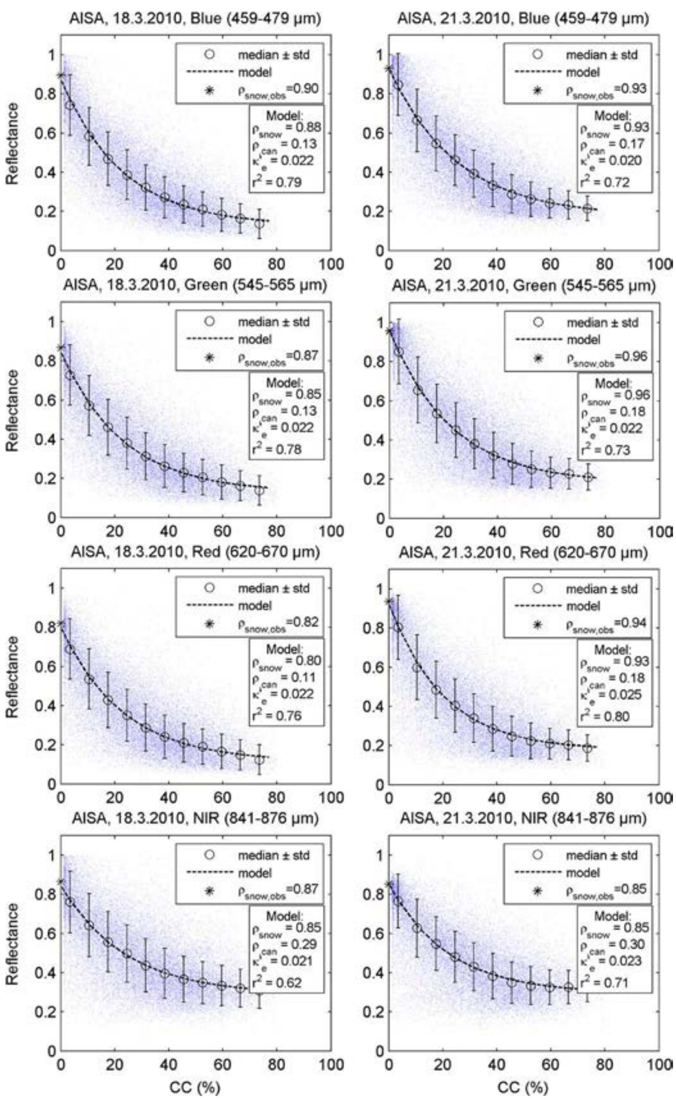

Fig. 6. Modeled spectral reflectance and airborne AISA observations as a function of CC in March 2010. The median and STD of discretized observed values as well as the model fit are depicted. The median of the observed reflectance values over nonforested areas, the modeled effective extinction coefficient, and the coefficient of determination between the observations and the model are also given.

B. SAR

Table VI summarizes the estimates of the active-microwave forest model against the observations of SnowSAR airborne and TSX spaceborne sensors. The results show very similar model performance when using CC and SV as the descriptive parameter for forest characteristics (FP). However, in all bands and polarizations, the coefficient of determination r^2 was always slightly higher and the RMSE lower when using CC as the forest parameter. The model performance was therefore slightly better when using CC.

Model estimates of backscattering against forest CC are depicted with observations from the SnowSAR acquisition on 7.2.2012 in Fig. 7 for all four SnowSAR channels. The observed backscattering over nonforested areas is also marked for each channel. Similarly as reflectivity values given for optical spectrometry results in Fig. 6, $\sigma^0_{\mathrm{snow,obs}}$ gives the median of the measured backscatter directly over nonforested pixels, whereas $\sigma^0_{\mathrm{snow,ret}}$ indicates surface backscattering predicted by the model fit. The correlation (r^2) is generally lower than for the optical forest model; this is largely explained by the relatively large scatter of the airborne SAR observations due to speckle. Model estimates follow well the median of the observations, with model bias typically not larger than ± 0.2 dB, but the standard deviation of the observed value was typically high (2–3 dB). The model estimate of ground surface backscatter can be seen to match well the measured values over open terrain, particularly for the Ku-band. Slight discrepancies can be observed at the X-band. A possible reason contributing to the discrepancy is differing soil characteristics, such as permittivity and roughness in forested and open terrain. These are known to significantly affect the level of backscattering (e.g., [70]). At the X-band, these effects may be more prominent due to the increased signal penetration in dry snow, compared with the higher frequency Ku-band signal.

Examples of model fits to three selected TSX acquisitions are shown in Fig. 8, illustrating the complexity of the interactions between soil and snow conditions and the forest canopy. The acquisition from 25.11.2011 is from the beginning of the snow season, when the ground was covered with a thin layer (5 cm) of dry snow. The acquisition from 10.2.2012 represents

TABLE VI

RESULTS OF ACTIVE-MICROWAVE FOREST MODEL ESTIMATES AGAINST SNOWSAR AND TERRASAR-X OBSERVATIONS (RMSE, BIAS, COEFFICIENT OF DETERMINATION, AND THE DIFFERENCE BETWEEN THE RETRIEVED AND THE OBSERVED SNOW BACKSCATTER IN OPEN AREAS) WHEN USING FP = CC AND FP = SV. ALL AVAILABLE TSX IMAGES BETWEEN THE 1ST OF DECEMBER AND THE 30TH OF APRIL (WHEN THE GROUND WAS COVERED WITH SNOW) WERE TAKEN INTO ACCOUNT WHEN CALCULATING THE STATISTICAL AVERAGES. RMSE AND BIAS WERE CALCULATED IN DECIBEL UNITS

Sensor	Band	Pol	CC				SV			
			RMSE	bias	r^2	$\sigma^0_{snow,obs} - \sigma^0_{snow,ret}$ (dB)	RMSE	bias	r^2	$\sigma^0_{snow,obs} - \sigma^0_{snow,ret}$ (dB)
SnowSAR	X	VV	2.80	-0.054	0.44	-0.36	2.84	-0.100	0.42	-0.36
	X	VH	2.50	0.435	0.41	-0.69	2.54	0.305	0.38	-0.69
	Ku	VV	2.75	-0.176	0.35	0.05	2.78	-0.184	0.33	0.05
	Ku	VH	2.03	0.079	0.48	0.00	2.09	-0.022	0.44	0.00
TerraSAR-X	X	VV	1.85	-0.15	0.36	-0.74	1.82	0.030	0.35	-0.15
	X	VH	1.80	-0.11	0.43	0.75	1.80	0.097	0.41	-0.14

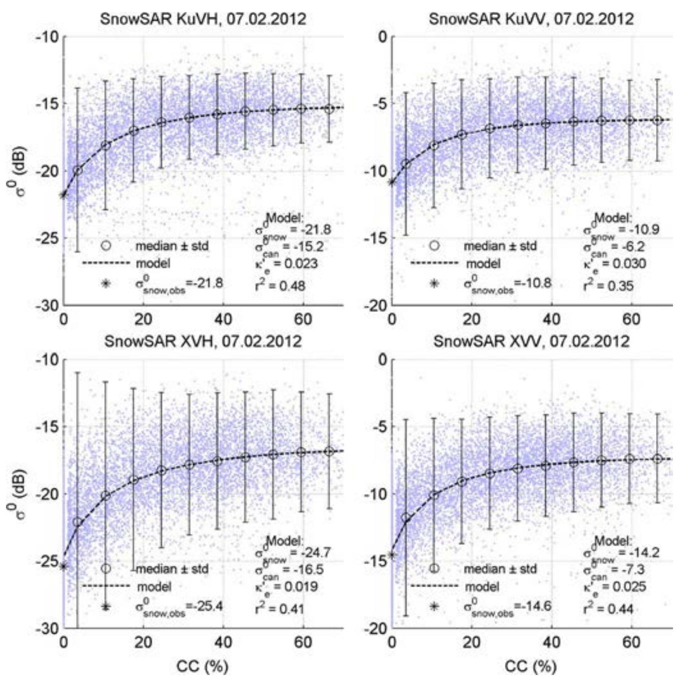

Fig. 7. Modeled backscattering in decibel units against observations from SnowSAR acquisition as a function of CC on 7.2.2012. The median and STD of discretized observed values in decibel units as well as the model fit are depicted. The median of the observed backscatter over nonforested areas, the modeled effective extinction coefficient, and the coefficient of determination between the observations and the model are also given for each channel. Top row: KuVh and KuVV channels. Bottom row: XVH and XVV channels.

mid-winter conditions, when dry snow covered the ground and the tree canopy. This was also temporally the closest TSX observation to the analyzed SnowSAR acquisition from 7.2.1012. The acquisition from 27.4.2012 represents a case at the beginning of the melting season, when the canopy was free of snow and the ground was covered with wet snow. For the 25.11.2011 and 10.2.2012 acquisitions, both $\sigma^0_{\text{snow,obs}}$ and $\sigma^0_{\text{snow,ret}}$ were relatively stable (to within 0.2 dB for both copolarization and cross-polarization indicating stable surface conditions). The effect of wet snow, presenting a low backscattering coefficient, is clearly seen as decreased $\sigma^0_{\text{snow,obs}}$ and $\sigma^0_{\text{snow,ret}}$ in the 27.4.2012 acquisition. The effect from forest canopy, however, is clearly different between the 25.11.2011 and 10.2.2012 acquisitions. The level of backscattering presented by dense canopy ($>$ 40% CC) is -10.9 and -16.8 dB for copolarization

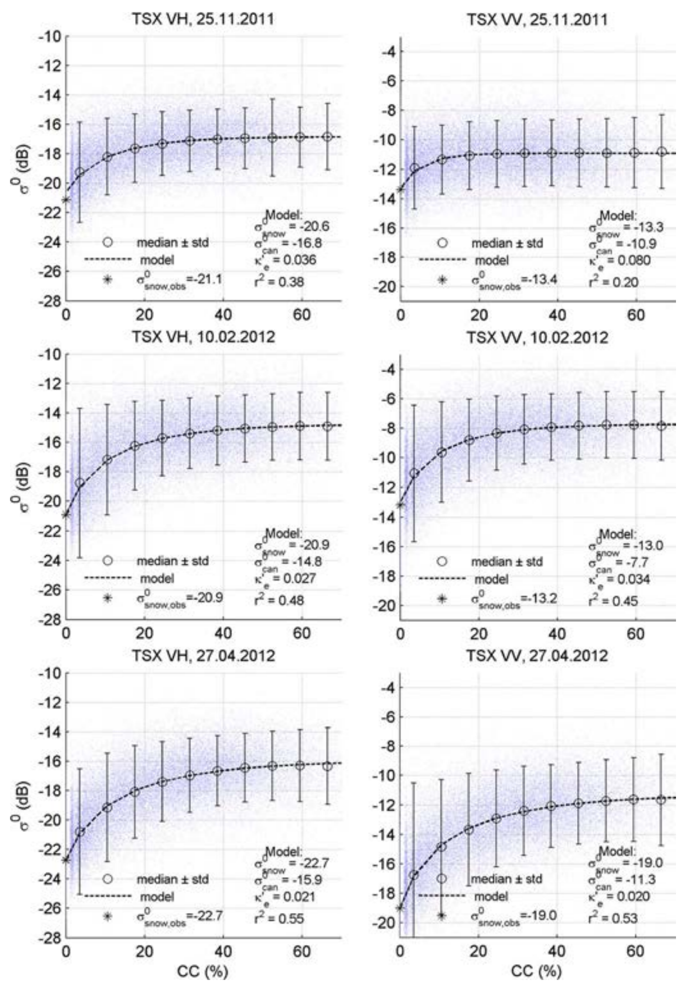

Fig. 8. Three examples of model estimates against TSX acquisitions. The median and STD of discretized observed values in decibel units as well as the model fit are depicted. The median of the observed backscatter over non-forested areas, the modeled effective extinction coefficient, and the coefficient of determination between the observations and the model are also given for each channel. The 25.11.2011 acquisition (top row) represents the beginning of the winter, when the snow layer is thin. The 10.2.2012 acquisition (center row) represents a typical winter snow condition, when the ground is covered with deep dry-snow layer. The 27.4.2012 acquisition (bottom row) represents melting season snow conditions, when the ground is covered with wet snow. VH-pol (left column) and VV-pol (right column).

and cross-polarization, respectively, for the 25.11.2011 acquisition. This level increased to -7.7 and -14.8 dB, respectively, for the 10.2.2012 acquisition.

Fig. 9. Photographs showing the snow conditions in Sodankylä on the same day as the selected TSX acquisitions in Fig. 8. At the time of the acquisition on 25.11.2011 (left), the temperature was a few degrees below 0 °C, and snow depth was 5 cm; on 10.2.2012 (middle), the temperature was below −15 °C, snow depth was 51 cm, and snow existed on the tree canopy; on 27.4.2012 (right), the temperature was a few degrees above 0 °C (wet snow), and snow depth was 61 cm.

Fig. 9 shows photographs taken from an automatic mast camera over the test area in Sodankylä from the same dates as the three TerraSAR-X acquisitions presented in Fig. 8. It can be seen that on 25.11.2011, the forest canopy was largely bare, whereas on 7.2.2012, the canopy was covered by accumulated snow.

The scattering of the TSX observations was smaller than the scattering of the SnowSAR observations, but still fairly larger than in the optical observations. The RMSE between the model and the TSX observations was typically smaller than ± 2 dB. The active-microwave forest model estimates follow well the median of the observations also in the case of the TSX sensor.

In Fig. 10, results of the TSX acquisitions are summarized in terms of a time series of the observed and modeled σ^0, κ^{l}_{e} and correlation between model and observations (r^2). *In situ* measurements of air temperature at 2-m height, soil temperature at 2-cm depth, and snow depth are also presented for the same time periods. During the snow season, the modeled canopy backscatter contribution was clearly higher (up to 7- and 8-dB difference for VV- and VH-pol, respectively) than the contribution of nonforested surface (snow), but before, or in the beginning of the snow season when the snow layer was still very thin, the backscatter contribution of canopy and ground/snow were almost the same (up to 1- and 3-dB difference for VV- and VH-pol, respectively), particularly at VV-pol. Consequently, during this period (before, or in the beginning of the snow season), the correlation between the model and observations was considerably lower (up to 0.35) than in the middle of the snow season. In the snowmelt season with wet-snow conditions, mostly the ground/snow backscatter $\sigma^0_{\mathrm{snow,ret}}$ and, in some extent, also the canopy backscatter σ^0_{can} were lower than $\sigma^0_{\mathrm{snow,ret}}$ and σ^0_{can} in dry-snow conditions (ground/snow: up to 8- and 4-dB difference between wet- and dry-snow conditions for VV- and VH-pol, respectively; canopy: up to 4- and 2-dB difference for VV- and VH-pol, respectively), and the correlation between the model and observations was as high, or even higher (up to 0.1 higher) than in the dry-snow season. Acquisitions with wet snow can therefore be recognized from sharp decrease of backscattering from nonforested surface, particularly in VV-pol. The modeled effective canopy extinction coefficient κ^{l}_{e} was typically higher when the difference between σ^0_{can} and $\sigma_{\mathrm{snow,ret}}$ was small, with the exception of wet-snow conditions, where κ^{l}_{e} was low regardless of the small difference between σ^0_{can} and $\sigma^0_{\mathrm{snow,ret}}$. The performance of the model was generally better with cross-polarization than with copolarization SAR, as the correlation between observations and the model with cross-polarization was typically higher (bottom row in Fig. 10).

C. Passive-Microwave Systems

Inversion of the passive-microwave model [see (9)], performed using the method outlined in Section III-D, was analyzed against airborne HUTRAD observations. Results comparing the statistics of model estimates to observations are summarized in Table VII, including the comparison of retrieved $T_{B,\mathrm{snow,ret}}$ to $T_{B,\mathrm{snow,obs}}$ in nonvegetated areas. When using FP = CC in the model, the RMSE was typically larger, and the correlation was lower than when using SV. However, these differences were marginal, and the overall model performance was nearly the same when using CC or SV, although SV has been mainly used in previous studies [38], [44].

Fig. 11 shows the observed and modeled brightness temperature for 10.65, 18.7, and 36.5 GHz, H- and V-pol, when using FP = SV. Parameters required to achieve a fit of the model, i.e., retrieved values ($T_{B,\mathrm{snow,ret}}$, T_{canopy}, $\kappa^{l}_{e,\mathrm{PM}}$) are also displayed. The best correlation, in terms of calculated r^2 values, was achieved for the two higher frequencies. This was largely due to the overall higher dynamics of the observed signal on these channels; the lowest correlation was observed for 10.65 GHz, V-pol, which showed also the weakest overall dynamics in the signal against vegetation conditions (SV). The results indicate that the presented zeroth-order model may not be applicable for the 10.65-GHz V-pol; the estimated total extinction for this channel was unrealistically high, indicating that the fit procedure yielded unsatisfactory results. Retrieved values of $T_{B,\mathrm{snow,ret}}$ reflected well the values observed over nonforested terrain $T_{B,\mathrm{snow,obs}}$, differing maximum 2 K for all observed channels. The resulting model predictions against forest canopy [see (9)] was compared with previous studies by replacing the one-way transmissivity [see (2)] by the transmissivity modeled in [38] and [44], while applying identical (measured) contributions for $T_{B,\mathrm{snow,obs}}$. Transmissivity for H-pol at 36.5 GHz was not provided in [38], and transmissivity for 10.65 GHz was not provided in [44]. Generally, the models

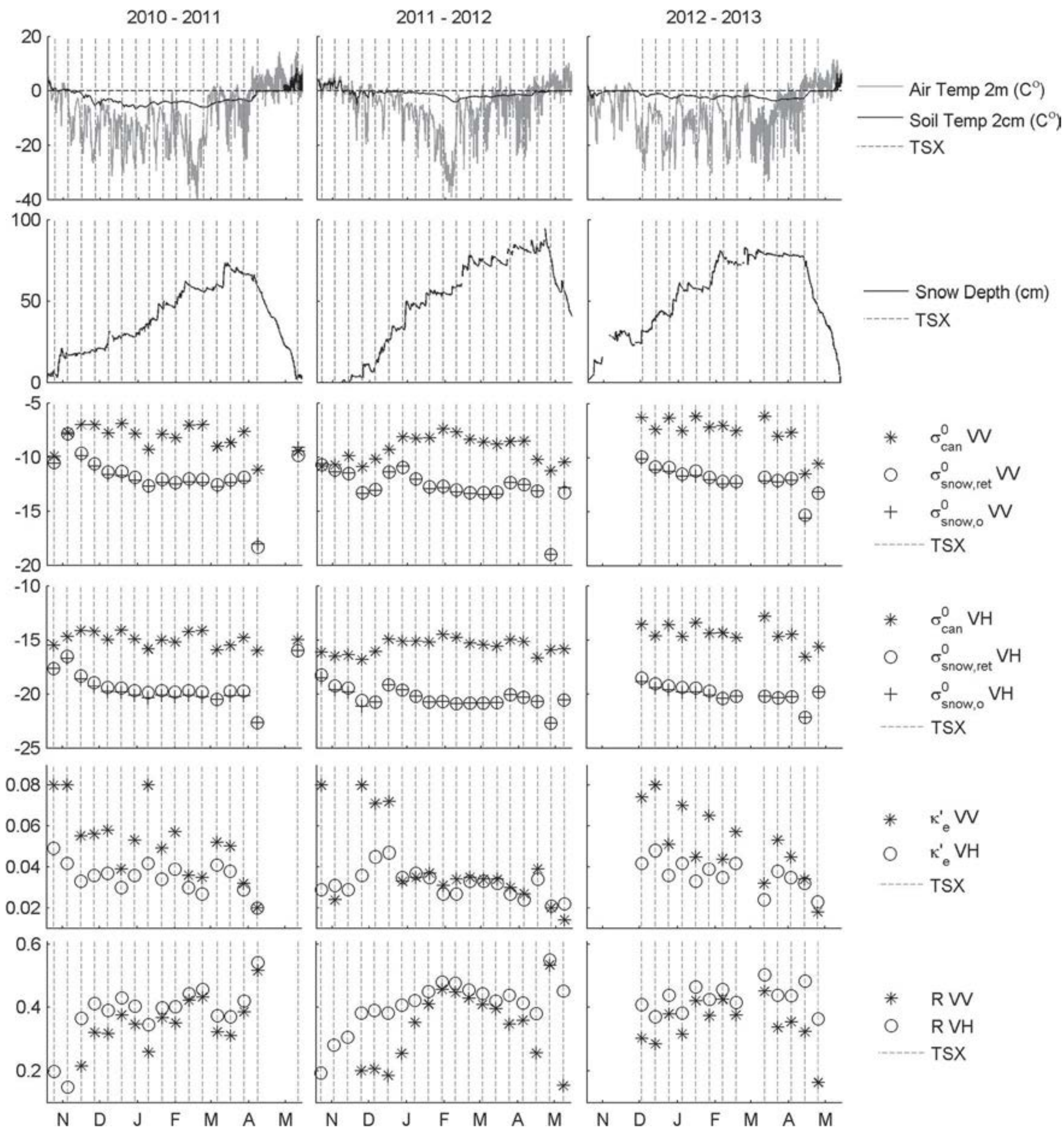

Fig. 10. (Top row) 2-m air temperature and 2-cm soil temperature during the observed periods in the test area. Second row from the top: Snow depth. Third row from the top: Backscatter of nonforested surface (snow or/and ground) based on observations ($\sigma^0_{\mathrm{snow},o}$) and model predicted backscatter of nonforested surface ($\sigma^0_{\mathrm{snow,ret}}$) and canopy ($\sigma^0_{\mathrm{can}}$) for VV-pol in decibel units. Fourth row from the top: Same for VH-pol. Fifth row from the top: Effective extinction coefficient (κ_e) for VV- and VH-pol. Bottom row: Coefficient of determination (r^2) between observed and modeled backscatter. The vertical dashed lines show the timing of the TSX acquisitions.

TABLE VII
RESULTS OF PASSIVE-MICROWAVE FOREST MODEL ESTIMATES AGAINST AIRBORNE HUTRAD RADIOMETER OBSERVATIONS (RMSE, BIAS, COEFFICIENT OF DETERMINATION, AND THE DIFFERENCE BETWEEN THE RETRIEVED AND THE OBSERVED SNOW BRIGHTNESS TEMPERATURE IN OPEN AREAS) WHEN USING FP = CC AND FP = SV

Band	Pol	CC				SV			
		RMSE	bias	r^2	$T_{B,snow,obs} - T_{B,snow,ret}$	RMSE	bias	r^2	$T_{B,snow,obs} - T_{B,snow,ret}$
10 GHz	V	1.33	-0.072	0.09	0.8	1.20	0.008	0.15	0.5
	H	2.21	0.008	0.72	-0.4	2.21	0.100	0.72	-0.7
18 GHz	V	1.89	-0.005	0.75	0.0	1.79	0.090	0.78	-0.1
	H	3.32	0.042	0.82	-0.1	3.21	0.141	0.83	-0.8
36 GHz	V	8.48	0.093	0.84	1.4	8.00	0.126	0.86	1.0
	H	10.54	0.116	0.84	1.9	10.00	0.154	0.86	1.2

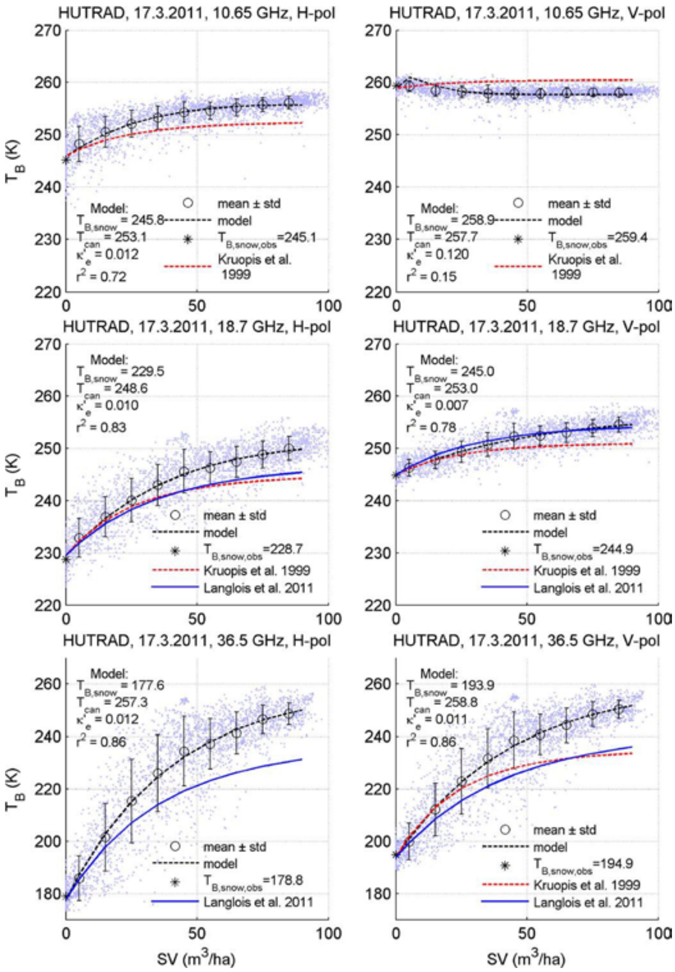

Fig. 11. Model estimates of brightness temperature versus airborne HUTRAD observations at 10.65, 18.7, and 36.5 GHz, H- and V-pol, as a function of SV. The mean and STD of discretized observed values as well as the model fits are depicted. The mean observed brightness temperature over dry non-forested areas, the modeled effective extinction coefficient, and the coefficient of determination between the observations and the model are also given for each channel. As a reference, the model [see (9)] was tested by replacing the transmissivity with the transmissivity modeled in [38] and [44].

in [38] and [44] gave a lower brightness temperature with increasing SV, compared with the fitted model provided here. An exception was the 18.7-GHz band V-pol, where the model in [44] provided a close fit with observations and the model of this study, and 10.65-GHz V-pol, where the model fit provided nonoptimal results.

V. Conclusion

In this paper, simplified zeroth-order models have been applied to simulate forest canopy effects on both optical and microwave remote sensing observations of snow-covered terrain. The models were tested against an experimental data set consisting of airborne and spaceborne observations over a test site in the northern boreal forest zone. Models were inverted using a numerical approach, by means of optimizing the model parameters for vegetation transmissivity as well as properties of the underlying surface against a large number of observations, providing a retrieved value for the signal level beneath the forest canopy. Simplified proxy parameters describing forest characteristics, namely, CC and SV, were derived from LiDAR scans of the test area. When successful, such an inversion allows the separation of forest contribution to the observation, which enables to single out the contribution of the medium beneath the canopy, which is the parameter sought by many applications of EO. Compared with more complex analytical models, simple zeroth-order models present minimal computational and ancillary data requirements and are therefore optimal for large-scale EO retrieval schemes. Similar model inversion has been previously applied successfully in, e.g., optical remote sensing of the SCA [15], [33], [71] and in SAR data analyses [20], [21], [36], [72].

The comparison of model estimates to observational data demonstrated that for the investigated microwave frequency bands and optical wavelengths, a zeroth-order model can estimate the range of extinction properties of electromagnetic signals in a boreal forest canopy to a high degree of accuracy. In particular, model estimates showed a high degree of correlation against HUTRAD passive-microwave and AISA airborne optical data, with r^2 values ranging from 0.7 to 0.9, depending on the observation spectral band and the day of observation (not including the 10-GHz band in passive microwave and the NIR band in optical). Moreover, for all sensor types, the retrieved estimate for the signal at the ground/snow level, beneath the forest canopy, was very close to the values observed for open terrain. This provides an indication that the demonstrated methodology can be used to compensate for effects of the forest cover, when investigating, e.g., properties of snow cover or soil.

The active-microwave model was able to successfully estimate the median of the observations, i.e., the bias was small, but the larger scatter of the observational data, typical for active-microwave sensors, was reflected by higher RMSE and lower correlation between the retrieved model and the observed values. Specifically, the SnowSAR airborne X- and Ku-band observations exhibited a high degree of variability due to observation speckle. An analysis of TerraSAR-X time series revealed some seasonal trends in the retrieved model fit parameters. That is, the backscattering contribution of the ground/snow was similar both in the retrieved model as well as for direct observations over nonforested terrain. This is again highly encouraging as it demonstrates that possible changes in canopy conditions were sufficiently addressed by the considerations of the zeroth-order model, despite radical changes in, e.g., snow conditions both in the ground/snow and on the forest canopy (see Figs. 8 and 9). In terms of r^2 values between the model and observations, reasonable correlations (up to over 0.7) were achieved during the dry-snow season and in early snowmelt season. In the early snow season and under advanced snowmelt conditions, the correlations were reduced (r^2 values under 0.5). As stated, these values reflect an overall larger scatter of the SAR observations when compared with both optical and passive microwave, which this is largely due to speckle effects typical for active-microwave measurements.

Model performance against airborne passive-microwave observations also showed a high correlation (up to 0.9) for two higher frequency bands observed (18.7 and 36.5 GHz). For a lower frequency (10.65 GHz), correlation was reduced, which is largely due to the inherent insensitivity to vegetation at this frequency band. The vertically polarized signal at this frequency showed possibly the effect of soil brightness temperature reflected from vegetation trunks; this hypothesis, however, requires further investigation. Nevertheless, ground/snow contribution (brightness temperature) from model inversion was very close to values observed over nonforested terrain for all frequency bands and both polarizations. SV has previously been used when modeling the effect of forest canopy on snow retrieval with passive-microwave sensors [38], [44]. However, here, the model performance when using CC as the forest parameter was nearly as good as when using SV. CC can therefore act as a good alternative to SV when the latter is not available. Although a retrieval method analogous to that applied in the case of optical and SAR data for snow parameter retrieval is not directly applicable for satellite microwave radiometer observations, which is mainly due to the coarse resolution of spaceborne sensors, the results show that zeroth-degree models have the potential to simulate the extinction properties of a typical boreal forest canopy, without the necessity of accounting for higher-order scattering effects. This study indicates some discrepancies against the models published in [38] and [44], which is widely applied in snow parameter retrieval algorithms, such as those in [24], [25], and [73] (see Fig. 11). Thus, following the results obtained here, a possible revision of the currently used inversion algorithms (also operational) for the mapping of SWE from spaceborne microwave radiometer data is required.

The results are of high relevance concerning practical applications for retrieval of snow-cover properties from EO satellites in the northern Hemisphere. Forward models applied in retrieval algorithms need to be relatively simple in nature due to both computational restrictions and, in particular, ancillary data requirements. Compared with models of higher order, the presented zeroth-order models satisfy both of these requirements. Furthermore, it was shown that a single parameter or proxy value describing the forest properties (either SV or CC) provided the necessary correlation with the observed signal dynamics, required to fit the models to observations. This is particularly encouraging as it implies that forest canopy effects can be regulated in retrieval algorithms even if complex multiple scattering effects are neglected; furthermore, compensation for canopy effects can be made using data that are already available or can be retrieved from other remote sensing observations.

ACKNOWLEDGMENT

The authors would like to thank the European Space Agency for providing the SnowSAR observations, the Finnish NLS for providing the LiDAR data, and the Natural Resources Institute Finland (LUKE) for providing the MS-NFI forest data. They would also like to thank Dr. T. Busche and Dr. I. Hajnsek from the German Aerospace Center (DLR) for providing the TerraSAR-X data and the Graduate School in Airborne Imaging Spectroscopy Application and Research in Earth Sciences (AISARES) for enabling the AISA instrument measurements.

REFERENCES

[1] P. Y. Groisman, T. R. Karl, and R. W. Knight, "Observed impact of snow cover on the heat balance and the rise of continental spring temperatures," *Science*, vol. 263, no. 5144, pp. 198–200, Jan. 1994.

[2] ACIA, Impact of a Warming Arctic: Arctic Climate Impact Assessment. Cambridge, U.K., Cambridge Univ. Press, 2004, [Accessed 02 11 2014]. [Online]. Available: http://www.acia.uaf.edu

[3] E. S. Euskirchen, A. D. McGuire, and F. S. Chapin, "Energy feedbacks of northern high-latitude ecosystems to the climate system due to reduced snow cover during 20th century warming," *Global Change Biol.*, vol. 13, no. 11, pp. 2425–2438, Nov. 2007.

[4] G. E. Liston and C. A. Hiemstra, "A simple data assimilation system for complex snow distributions (SnowAssim)," *J. Hydrometeorol.*, vol. 9, no. 5, pp. 989–1004, Oct. 2008.

[5] A. W. Nolin, "Recent advances in remote sensing of seasonal snow," *J. Glaciol.*, vol. 56, no. 200, pp. 1141–1150, Dec. 2010.

[6] A. J. Dietz, C. Kuenzer, U. Gessner, and S. Dech, "Remote sensing of snow—A review of available methods," *Int. J. Remote Sens.*, vol. 33, no. 13, pp. 4094–4134, Jul. 2012.

[7] A. Frei *et al.*, "A review of global satellite-derived snow products," *Adv. Space Res.—Oceanogr., Cryosp. Freshwater Flux Ocean*, vol. 50, no. 8, pp. 1007–1029, Oct. 2012.

[8] D. K. Hall, G. A. Riggs, V. V. Salomonson, N. E. DiGirolamo, and K. J. Bayr, "MODIS snow-cover products," *Remote Sens. Environ.*, vol. 83, no. 1/2, pp. 181–194, Nov. 2002.

[9] T. H. Painter, J. Dozier, D. A. Roberts, R. E. Davis, and R. O. Green, "Retrieval of subpixel snow-covered area and grain size from imaging spectrometer data," *Remote Sens. Environ.*, vol. 85, no. 1, pp. 64–77, Apr. 2003.

[10] D. Vikhamar and R. Solberg, "Subpixel mapping of snow cover in forests by optical remote sensing," *Remote Sens. Environ.*, vol. 84, no. 1, pp. 69–82, Jan. 2003.

[11] D. Vikhamar and R. Solberg, "Snow-cover mapping in forests by constrained linear spectral unmixing of MODIS data," *Remote Sens. Environ.*, vol. 88, no. 3, pp. 309–323, Dec. 2003.

[12] V. V. Salomonson and I. Appel, "Estimating fractional snow cover from MODIS using the normalized difference snow index," *Remote Sens. Environ.*, vol. 89, no. 3, pp. 351–360, Feb. 2004.

[13] V. Salomonson and I. Appe, "Development of the Aqua MODIS NDSI fractional snow cover algorithm and validation results," *IEEE Trans. Geosci. Remote Sens.*, vol. 44, no. 7, pp. 1747–1756, Jul. 2006.

[14] S. J. Metsämäki, S. T. Anttila, H. J. Markus, and J. M. Vepsäläinen, "A feasible method for fractional snow cover mapping in boreal zone based on a reflectance model," *Remote Sens. Environ.*, vol. 95, no. 1, pp. 77–95, Mar. 2005.

[15] S. Metsämäki *et al.*, "An optical reflectance model-based method for fractional snow cover mapping applicable to continental scale," *Remote Sens. Environ.*, vol. 123, pp. 508–521, Aug. 2012.

[16] D. K. Hall and G. A. Riggs, "Accuracy assessment of the MODIS snow products," *Hydrol. Process.*, vol. 21, no. 12, pp. 1534–1547, Jun. 2007.

[17] J. Dozier, R. O. Green, A. W. Nolin, and T. H. Painter, "Interpretation of snow properties from imaging spectrometry," *Remote Sens. Environ.*, vol. 113, no. S1, pp. S25–S37, Sep. 2009.

[18] J. Yang *et al.*, "Evaluation of snow products over the Tibetan Plateau," *Hydrol. Process.*, to be published.

[19] T. Nagler and H. Rott, "Retrieval of wet snow by means of multitemporal SAR data," *IEEE Trans. Geosci. Remote Sens.*, vol. 38, no. 2, pp. 754–765, Mar. 2000.

[20] K. P. Luojus, J. T. Pulliainen, S. J. Metsamaki, and M. T. Hallikainen, "Snow-covered area estimation using satellite radar wide-swath images," *IEEE Trans. Geosci. Remote Sens.*, vol. 45, no. 4, pp. 978–989, Apr. 2007.

[21] K. P. Luojus, J. T. Pulliainen, S. J. Metsamaki, and M. T. Hallikainen, "Enhanced SAR-based snow-covered area estimation method for boreal forest zone," *IEEE Trans. Geosci. Remote Sens.*, vol. 47, no. 3, pp. 922–935, Mar. 2009.

[22] A. T. C. Chang, J. L. Foster, and D. K. Hall, "Satellite sensor estimates of northern hemisphere snow volume," *Int. J. Remote Sens.*, vol. 11, no. 1, pp. 167–171, Jan. 1990.

[23] R. E. Kelly, A. T. Chang, L. Tsang, and J. L. Foster, "A prototype AMSR-E global snow area and snow depth algorithm," *IEEE Trans. Geosci. Remote Sens.*, vol. 41, no. 2, pp. 230–242, Feb. 2003.

[24] J. Pulliainen, "Mapping of snow water equivalent and snow depth in boreal and sub-arctic zones by assimilating space-borne microwave radiometer data and ground-based observations," *Remote Sens. Environ.*, vol. 101, no. 2, pp. 257–269, Mar. 2006.

[25] M. Takala *et al.*, "Estimating northern hemisphere snow water equivalent for climate research through assimilation of space-borne radiometer data and ground-based measurements," *Remote Sens. Environ.*, vol. 115, no. 12, pp. 3517–3529, Dec. 2011.

[26] M. Takala, J. Pulliainen, S. J. Metsamaki, and J. T. Koskinen, "Detection of snowmelt using spaceborne microwave radiometer data in Eurasia from 1979 to 2007," *IEEE Trans. Geosci. Remote Sens.*, vol. 47, no. 9, pp. 2996–3007, Sep. 2009.

[27] X. Li, A. H. Strahler, and C. E. Woodcock, "A hybrid geometric optical-radiative transfer approach for modeling albedo and directional reflectance of discontinuous canopies," *IEEE Trans. Geosci. Remote Sens.*, vol. 33, no. 2, pp. 466–480, Mar. 1995.

[28] M. Schlerf and C. Atzberger, "Inversion of a forest reflectance model to estimate structural canopy variables from hyperspectral remote sensing data," *Remote Sens. Environ.*, vol. 100, no. 3, pp. 281–294, Feb. 2006.

[29] J. Liu *et al.*, "Modeling the view angle dependence of gap fractions in forest canopies: Implications for mapping fractional snow cover using optical remote sensing," *J. Hydrometeorol.*, vol. 9, no. 5, pp. 1005–1019, Oct. 2008.

[30] M. Salminen, J. Pulliainen, S. Metsämäki, A. Kontu, and H. Suokanerva, "The behaviour of snow and snow-free surface reflectance in boreal forests: Implications to the performance of snow covered area monitoring," *Remote Sens. Environ.*, vol. 113, no. 5, pp. 907–918, May 2009.

[31] K. Niemi *et al.*, "The behaviour of mast-borne spectra in a snow-covered boreal forest," *Remote Sens. Environ.*, vol. 124, pp. 551–563, Sep. 2012.

[32] K. Heinilä *et al.*, "The effect of boreal forest canopy to reflectance of snow covered terrain based on airborne imaging spectrometer observations," *Int. J. Appl. Earth Observ. Geoinf.*, vol. 27, pt. A, pp. 31–41, Apr. 2014.

[33] J. Pulliainen, M. Salminen, K. Heinilä, J. Cohen, and H. Hannula, "Semi-empirical modeling of the scene reflectance of snow-covered boreal forest: Validation with airborne spectrometer and LIDAR observations," *Remote Sens. Environ.*, vol. 155, pp. 303–311, Dec. 2014.

[34] F. T. Ulaby, *Microwave Remote Sensing Active and Passive. 3 From Theory to Applications*. Dedham, MA, USA: Artech House, 1986.

[35] J. T. Pulliainen, "Backscattering properties of boreal forests at the C- and X-bands," *IEEE Trans. Geosci. Remote Sens.*, vol. 32, no. 5, pp. 1041–1050, Sep. 1994.

[36] T. Pulliainen, L. Kurvonen, and M. T. Hallikainen, "Multitemporal behavior of L- and C-band SAR observations of boreal forests," *IEEE Trans. Geosci. Remote Sens.*, vol. 37, no. 2, pp. 927–937, Mar. 1999.

[37] J. Koskinen and M. Hallikainen, "The use of ERS-1 SAR data for snow melt detection," *Phys. Chem. Earth*, vol. 22, no. 3/4, pp. 285–289, 1997.

[38] N. Kruopis *et al.*, "Passive microwave measurements of snow-covered forest areas in EMAC'95," *IEEE Trans. Geosci. Remote Sens.*, vol. 37, no. 6, pp. 2699–2705, Nov. 1999.

[39] P. Pampaloni, "Microwave radiometry of forests," *Waves Random Media*, vol. 14, no. 2, pp. S275–S298, Apr. 2004.

[40] C. Derksen, A. Walker, and B. Goodison, "Evaluation of passive microwave snow water equivalent retrievals across the boreal forest/tundra transition of western Canada," *Remote Sens. Environ.*, vol. 96, no. 3/4, pp. 315–327, Jun. 2005.

[41] J. L. Foster *et al.*, "Quantifying the uncertainty in passive microwave snow water equivalent observations," *Remote Sens. Environ.*, vol. 94, no. 2, pp. 187–203, Jan. 2005.

[42] M. Pardé, K. Goita, R. Royer, and F. Vachon, "Boreal forest transmissivity in the microwave domain using ground-based measurements," *IEEE Geosci. Remote Sens. Lett.*, vol. 2, no. 2, pp. 169–171, Apr. 2005.

[43] J. Lemmetyinen *et al.*, "A comparison of airborne microwave brightness temperatures and snowpack properties across the boreal forests of Finland and western Canada," *IEEE Trans. Geosci. Remote Sens.*, vol. 47, no. 3, pp. 965–978, Mar. 2009.

[44] A. Langlois *et al.*, "Improved corrections of forest effects on passive microwave satellite remote sensing of snow over boreal and subarctic regions," *IEEE Trans. Geosci. Remote Sens.*, vol. 49, no. 10, pp. 3824–3837, Oct. 2011.

[45] F. T. Ulaby, C. T. Allen, G. Eger, III, and E. Kanemasu, "Relating the microwave backscattering coefficient to leaf area index," *Remote Sens. Environ.*, vol. 14, no. 1–3, pp. 113–133, Jan. 1984.

[46] A. Freeman, J. Villasenor, J. D. Klein, P. Hoogeboom, and J. Groot, "On the use of multi-frequency and polarimetric radar backscatter features for classification of agricultural crops," *Int. J. Remote Sens.*, vol. 15, no. 9, pp. 1799–1812, Jun. 1994.

[47] S. Twomey, H. Jacobowitz, and H. B. Howell, "Matrix methods for multiple-scattering problems," *J. Atmos. Sci.*, vol. 23, no. 3, pp. 289–298, May 1966.

[48] H. J. Eom and A. K. Fung, "A scatter model for vegetation up to Ku-band," *Remote Sens. Environ.*, vol. 15, no. 3, pp. 185–200, Jun. 1984.

[49] F. T. Ulaby, K. Sarabandi, K. McDonald, M. Whitt, and M. C. Dobson, "Michigan microwave canopy scattering model," *Int. J. Remote Sens.*, vol. 11, no. 7, pp. 1223–1253, Jun. 1990.

[50] M. A. Karam, A. K. Fung, R. H. Lang, and N. S. Chauhan, "A microwave scattering model for layered vegetation," *IEEE Trans. Geosci. Remote Sens.*, vol. 30, no. 4, pp. 767–784, Jul. 1992.

[51] P. Ferrazzoli and L. Guerriero, "Radar sensitivity to tree geometry and woody volume: A model analysis," *IEEE Trans. Geosci. Remote Sens.*, vol. 33, no. 2, pp. 360–371, Mar. 1995.

[52] G. Cookmartin *et al.*, "Modeling microwave interactions with crops and comparison with ERS-2 SAR observations," *IEEE Trans. Geosci. Remote Sens.*, vol. 38, no. 2, pp. 658–670, Mar. 2000.

[53] G. Macelloni, S. Paloscia, P. Pampaloni, F. Marliani, and M. Gai, "The relationship between the backscattering coefficient and the biomass of narrow and broad leaf crops," *IEEE Trans. Geosci. Remote Sens.*, vol. 39, no. 4, pp. 873–884, Apr. 2001.

[54] G. Macelloni, M. Brogioni, F. Montomoli, and G. Fontanelli, "Effect of forests on the retrieval of snow parameters from backscatter measurements," *Eur. J. Remote Sens.*, vol. 45, no. 1, pp. 121–132, 2012.

[55] R. Magagi, M. Bernier, and M.-C. Bouchard, "Use of ground observations to simulate the seasonal changes in the backscattering coefficient of the subarctic forest," *IEEE Trans. Geosci. Remote Sens.*, vol. 40, no. 2, pp. 281–297, Feb. 2002.

[56] P. Liang, L. E. Pierce, and M. Moghaddam, "Radiative transfer model for microwave bistatic scattering from forest canopies," *IEEE Trans. Geosci. Remote Sens.*, vol. 43, no. 11, pp. 2470–2483, Nov. 2005.

[57] F. Montomoli *et al.*, "Observations and simulation of multi frequency SAR data over a snow-covered boreal forest," *IEEE J. Sel. Topics Appl. Earth Observ. Remote Sens.*, to be published.

[58] J. S. Lee, M. R. Grunes, E. Pottier, and L. Ferro-Famil, "Unsupervised terrain classification preserving polarimetric scattering characteristics," *IEEE Trans. Geosci. Remote Sens.*, vol. 42, no. 4, pp. 722–731, Apr. 2004.

[59] L. Thirion, I. Chênerie, and C. Galy, "Application of a coherent model in simulating the backscattering coefficient of a mangrove forest," *Waves Random Media*, vol. 14, no. 2, pp. S299–S316, Apr. 2004.

[60] X. Li and A. H. Strahler, "Geometric-optical modeling of a conifer forest canopy," *IEEE Trans. Geosci. Remote Sens.*, vol. GE-23, no. 5, pp. 705–721, Sep. 1985.

[61] T. H. Painter *et al.*, "Retrieval of subpixel snow covered area, grain size, and albedo from MODIS," *Remote Sens. Environ.*, vol. 113, no. 4, pp. 868–879, Apr. 2009.

[62] A. G. Klein, D. K. Hall, and G. A. Riggs, "Improving snow cover mapping in forests through the use of a canopy reflectance model," *Hydrol. Process.*, vol. 12, no. 10/11, pp. 1723–1744, Sep. 1998.

[63] A. Rosema, W. Verhoef, H. Noorbergen, and J. J. Borgesius, "A new forest light interaction model in support of forest monitoring," *Remote Sens. Environ.*, vol. 42, no. 1, pp. 23–41, Oct. 1992.

[64] H. Rott *et al.*, "Cold regions hydrology high-resolution observatory for snow and cold land processes," *Proc. IEEE*, vol. 98, no. 5, pp. 752–765, May 2010.

[65] Vuodenajat tilastoin, Finnish Meteorological Institute (Ilmatieteen Laitos), Helsinki, Finland, 2014, [Accessed 22 10 2014]. [Online]. Available: http://ilmatieteenlaitos.fi/vuodenaikojen-tilastot

[66] D. Di Leo, A. Coccia, and A. Meta, "Technical assistance for the development of an X- to ku-band MiniSAR airborne system; Radiometric calibration of SnowSAR images," MetaSensing, Noordwijk, The Netherlands, Tech. Note MS-EST-SNW-03-TCN2_032, 3.2, 2014.

[67] E. Tomppo, M. Haakana, M. Katila, and J. Peräsaari, *Multi-Source National Forest Inventory: Methods and Applications*. Dordrecht, The Netherlands: Springer-Verlag, 2008.

[68] J. Repola, and K. Ahnlund Ulvcrona, "Modelling biomass of young and dense Scots pine (Pinus sylvestris L.) dominated mixed forests in northern Sweden," *Silva Fenn.*, vol. 48, no. 5, p. 1190, Dec. 2014.

[69] J. Pulliainen, J. Koskinen, and M. Hallikainen, "Compensation of forest canopy effects in the estimation of snow covered area from SAR data," in *Proc. IEEE IGARSS*, Sydney, NSW, Australia, 2001, pp. 813–815.

[70] Y. Oh, K. Sarabandi, and F. T. Ulaby, "An empirical model and an inversion technique for radar scattering from bare soil surfaces," *IEEE Trans. Geosci. Remote Sens.*, vol. 30, no. 2, pp. 370–381, Mar. 1992.

[71] S. Metsämäki *et al.*, "Introduction to GlobSnow snow extent products with considerations for accuracy assessment," *Remote Sens. Environ.*, vol. 156, pp. 96–108, Jan. 2015.

[72] J. T. Koskinen, J. T. Pulliainen, K. P. Luojus, and M. Takala, "Monitoring of snow-cover properties during the spring melting period in forested areas," *IEEE Trans. Geosci. Remote Sens.*, vol. 48, no. 1, pp. 50–58, Jan. 2010.

[73] J. Pulliainen and M. Hallikainen, "Retrieval of regional snow water equivalent from space-borne passive microwave observations," *Remote Sens. Environ.*, vol. 75, no. 1, pp. 76–85, Jan. 2001.